

Implantation studies of low-energy positive muons in niobium thin films

Ryan M. L. McFadden,^{1,2,*} Andreas Suter,^{3,†} Leon Ruf,⁴ Angelo Di Bernardo,^{4,5}
Arnold M. Müller,⁶ Thomas Prokscha,³ Zaher Salman,³ and Tobias Junginger^{1,2}

¹TRIUMF, 4004 Wesbrook Mall, Vancouver, BC V6T 2A3, Canada

²Department of Physics and Astronomy, University of Victoria,
3800 Finnerty Road, Victoria, BC V8P 5C2, Canada

³PSI Center for Neutron and Muon Sciences CNM, Forschungsstrasse 111, 5232 Villigen PSI, Switzerland

⁴Department of Physics, University of Konstanz, Universitaetsstrasse 10, 78464 Konstanz, Germany

⁵Department of Physics, University of Salerno, Via Giovanni Paolo II 132, 84084 Fisciano SA, Italy

⁶Laboratory of Ion Beam Physics, ETH Zurich, HPK H32 Otto-Stern-Weg 5, 8093 Zurich, Switzerland

(Dated: July 8, 2025)

Here we study the range of keV positive muons μ^+ implanted in $\text{Nb}_2\text{O}_5(x \text{ nm})/\text{Nb}(y \text{ nm})/\text{SiO}_2(300 \text{ nm})/\text{Si}$ [$x = 3.6 \text{ nm}, 3.3 \text{ nm}; y = 42.0 \text{ nm}, 60.1 \text{ nm}$] thin films using low-energy muon spin spectroscopy (LE- μ SR). At implantation energies $1.3 \text{ keV} \leq E \leq 23.3 \text{ keV}$, we compare the measured diamagnetic μ^+ signal fraction f_{dia} against predictions derived from implantation profile simulations using the TRIM.SP Monte Carlo code. Treating the implanted μ^+ as light protons p^+ , we find that simulations making use of updated stopping cross section data are in good agreement with the LE- μ SR measurements, in contrast to parameterizations found in earlier tabulations. Implications for other studies relying on accurate μ^+ stopping information are discussed.

I. INTRODUCTION

The positive muon μ^+ (spin $S_\mu = 1/2$; gyromagnetic ratio $\gamma_\mu/(2\pi) = 135.538\,809\,4(30) \text{ MHz T}^{-1}$ [1]; mean lifetime $\tau_\mu = 2.196\,981\,1(22) \mu\text{s}$ [2]; mass $m_\mu = 0.113\,428\,925\,9(25) \text{ u}$ [1]) finds widespread use in the study of condensed matter, with the leptonic elementary particle serving as muon spin spectroscopy's (μ SR) sensitive “spin probe” [3]. In μ SR, implanted μ^+ are used to monitor the local electromagnetic environment in a target of interest, analogous to “conventional” nuclear magnetic resonance (NMR) measurements using stable nuclei (see, e.g., [4]). Naturally, the range of applications is quite broad, and with over half-a-century of development and refinement [5], μ SR is now routinely applied to challenging problems [6] in physics, chemistry, and materials science (see, e.g., [7–10]).

In the last few decades, the capabilities of μ SR have been expanded to the realm of nanoscience through the development of a contemporary variant called low-energy μ SR (LE- μ SR) [11, 12]. LE- μ SR's key feature is the use of μ^+ beams with precisely controlled implantation energies $E \lesssim 30 \text{ keV}$, which imparts the variant with *spatial-resolution* over subsurface depths on the order of 10s to 100s of nanometers [13]. With the exception of a few complementary [14] techniques (e.g., β -radiation-detected NMR [15, 16]), LE- μ SR offers a unique combination of electromagnetic and spatial sensitivity, making it ideally suited for the study of exotic (sub)surface phenomenon (see, e.g., [17–25]). Though quite diverse in scope, these studies all share a common trait: they make explicit use of μ^+ 's E -dependent stopping distribution $\rho(z, E)$ to extract spatial information from the analysis.

Generally, information on $\rho(z, E)$ is not derived directly from a LE- μ SR measurement (cf. [12]), meaning it must be ob-

tained through alternative means. The most common approach is through separate simulations of the implantation process, with Monte Carlo binary collision approximation (BCA) codes (e.g., SRIM [26] or TRIM.SP [27–29]) being widely used for this purpose [30]. As the interaction of μ^+ with matter follows that of a *very* light proton p^+ ($m_\mu/m_{p^+} \approx 1/9$), it is possible to leverage what is known about p^+ implantation [26, 28, 31, 32] and adapt such codes for μ^+ implantation [13]. While such simulations have been shown to accurately reproduce the μ^+ range in metals such as Al, Cu, Ag, and Au [13, 33], similar checks in other elements remain lacking — particularly those where experimental stopping data is either sparse (e.g., Na, Ru, or Eu) or absent (e.g., Ho, Rh, or Pr) [34, 35]. Though this lack of data can be mitigated to some extent through contemporary predictive techniques (see, e.g., [36–39]), *experimental verification* remains the best means of achieving the accuracy desired for depth-resolved LE- μ SR measurements.

To illustrate the impact of accurate stopping profiles, we consider the elemental metal Nb. Despite being one of the most widely studied superconductors, interest in interrogating its physical properties (especially using implanted spin probes [40]) remains strong, largely due to the element's importance for superconducting radio frequency (SRF) technologies [41]. LE- μ SR has contributed to understanding the element's intrinsic Meissner response [42, 43], along with how it is modified through different surface treatments [44–47] or coatings [48]. For this purpose, accurate knowledge of $\rho(z, E)$ is crucial, as it dictates the absolute value of the superconducting length scales derived from the measurements. It is apparent that early LE- μ SR measurements (see, e.g., [42, 44]) find Nb's London penetration depth λ_L to be considerably shorter than older, widely cited estimates (see, e.g., [49]), suggesting the discrepancy may be *systematic* in origin.

Recently, it was suggested in Ref. [45] that refinements to the longstanding tabulations of Varelas-Biersack [50] coefficients describing p^+ stopping in Nb [31, 32], which are used by TRIM.SP [27–29], were possible through evaluation of the International Atomic Energy Agency's (IAEA) database on

* E-mail: rmlm@triumf.ca

† E-mail: andreas.suter@psi.ch

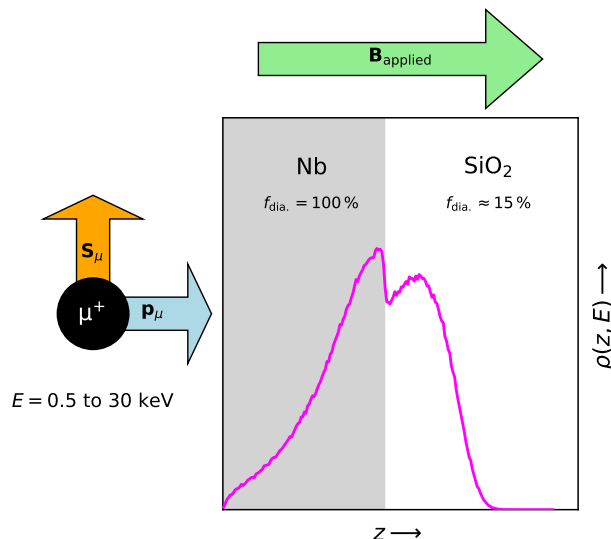


FIG. 1. Sketch of the μ^+ implantation experiment using LE- μ SR. Muons with their spin direction \mathbf{S}_μ perpendicular to their momentum \mathbf{p}_μ are implanted in Nb/ SiO_2 films at energies $E \in [0.5, 30]$ keV, such that their stopping profile $\rho(z, E)$ overlaps with the two material layers. An external magnetic field $\mathbf{B}_{\text{applied}} \approx 10 \text{ mT} \parallel \hat{z}$ is applied perpendicular to \mathbf{S}_μ , such that only the fraction of μ^+ stopped in a diamagnetic environment $f_{\text{dia.}}$ is observable. As $f_{\text{dia.}}$ deviates significantly between the two layers (see the sketch’s inset), the LE- μ SR signal amplitude is expected to decrease as more μ^+ stop in the SiO_2 layer.

electronic stopping powers [34, 35]. Specifically, using all available stopping data [51–54] (apart from a dataset of clear outliers [55]), a new Varelas-Biersack [50] parameterization was proposed [45], yielding magnetic penetration depths derived from LE- μ SR consistent with Nb’s clean-limit value $\sim 29 \text{ nm}$ (see, e.g., [45, 56]). While this agreement implies the correctness of the refined $\rho(z, E)$ simulations, no independent check was performed.

In this work, we expand upon the $\rho(z, E)$ refinements suggested in Ref. [45] and study the range of μ^+ in Nb using LE- μ SR. Following the approach in Refs. [13, 33], we implant μ^+ in Nb films deposited on amorphous SiO_2 for a span of energies E that result in $\rho(z, E)$ s which overlap the two layers. To determine the μ^+ stopping environment, we exploit the well-known property that, upon thermalization, all implanted μ^+ end up in a diamagnetic environment in metals, characterized by a Larmor frequency:

$$\omega_\mu = \gamma_\mu B, \quad (1)$$

where B is the local magnetic flux density at the μ^+ stopping site. By contrast, in the wide-gap insulator SiO_2 the majority of μ^+ bind with a “free” electron e^- (e.g., those liberated during the implantation process) to form the paramagnetic atomic-like state muonium ($\text{Mu} \equiv \mu^+ + e^-$), whose much larger gyromagnetic ratio $\gamma_{\text{Mu}} \approx 103\gamma_\mu$ makes it spectroscopically distinct from diamagnetic μ^+ . In modest magnetic fields $B \gtrsim 10 \text{ mT}$, spin-precession of the paramagnetic fraction is fast enough that, in the absence of specialized instrumentation

providing high time-resolution, it manifests as a *loss* of signal, with only the small diamagnetic fraction $f_{\text{dia.}} \approx 15\%$ [13, 57–60] in SiO_2 remaining observable. A sketch of the experiment is given in Figure 1. By comparing the evolution of the LE- μ SR signal amplitude vs. E in several Nb/ SiO_2 films against results from μ^+ implantation simulations, we find that a refined stopping power parameterization is necessary to accurately reproduce the μ^+ range in Nb.

II. EXPERIMENT

A. Samples

In the present study, we make use of two Nb films: one thin and another thicker sample, each deposited on $\text{SiO}_2(300 \text{ nm})/\text{Si}$ (n -doped, $\sim 50 \Omega \text{ cm}$) substrates (lateral dimensions of $\sim 2.5 \text{ cm} \times 2.5 \text{ cm}$ and $\sim 3 \text{ cm} \times 2 \text{ cm}$ for the thinner and thicker samples, respectively). Both films were grown in an ultra-high vacuum (UHV) chamber using a combination of direct current (DC) and radio frequency (RF) magnetron sputtering from three Nb targets (purity $> 99.995\%$). The chamber’s base (residual) pressure before growth was lower than 5.0×10^{-9} Torr and an Ar pressure of 3 mTorr was used during deposition of the Nb films with a power of 250 W applied to each Nb target. These settings yielded a deposition rate of $\sim 0.4 \text{ nm s}^{-1}$. Following synthesis, film thickness were confirmed independently by x-ray reflection (XRR) and Rutherford backscattering (RBS) measurements (see Appendix A), revealing slightly thinner dimensions for the Nb layer and the presence of a thin surface niobium pentoxide [$\text{Nb}_2\text{O}_5(3.3 \text{ nm})/\text{Nb}(42.0 \text{ nm})/\text{SiO}_2$ and $\text{Nb}_2\text{O}_5(3.6 \text{ nm})/\text{Nb}(60.1 \text{ nm})/\text{SiO}_2$ for the thinner and thicker films, respectively].

B. LE- μ SR Measurements

LE- μ SR measurements were performed at the Swiss Muon Source ($S_\mu S$) in the Paul Scherrer Institute (PSI), located in Villigen, Switzerland. Using the $\mu E4$ beamline [61], a $\sim 100\%$ spin-polarized μ^+ beam (intensity of $\sim 10^4 \text{ s}^{-1}$) was generated by moderating a $\sim 4 \text{ MeV}$ “surface” μ^+ beam using a film of condensed cryogenic gas [62, 63] and electrostatically re-accelerating the eluting epithermal ($\sim 15 \text{ eV}$) muons to $\sim 10 \text{ keV}$ or $\sim 15 \text{ keV}$. The beam was delivered to a dedicated spectrometer [61, 64, 65] using electrostatic optics housed within an UHV beamline, with the μ^+ arrival times triggered on a thin ($\sim 8 \text{ nm}$) carbon foil detector. Note that passage through the foil results in both a slight reduction in the beam’s mean kinetic energy ($\sim 1 \text{ keV}$) and introduces a small (asymmetric) energy spread ($\sim 450 \text{ eV}$). Control over the μ^+ implantation energy (and the μ^+ stopping depth) is achieved by biasing an electrically isolated sample holder using a high-voltage (HV) power supply. The beam was implanted into the Nb/ SiO_2 films affixed to the spectrometer’s cryostat, which was maintained at 200 K during the measurements (i.e., to mitigate the accumulation of

water atop the film's surface at the sample chamber's pressure $<10^{-7}$ mbar).

In LE- μ SR, the temporal evolution of the β -decay asymmetry $\mathcal{A}(t)$, is monitored using a set of decay positron detectors i surrounding the sample environment. The measured \mathcal{A} is proportional to the spin-polarization of the μ^+ ensemble:

$$P_\mu(t) \equiv \langle S_{\mu,\perp} \rangle / S_\mu,$$

where $\langle S_{\mu,\perp} \rangle / S_\mu \in [-1, 1]$ is the (normalized) expectation value transverse to the applied field. The count rate in a single detector N_i is given by:

$$N_i(t) = N_{0,i} \exp\left(-\frac{t}{\tau_\mu}\right) [1 + \mathcal{A}_i(t)] + b_i, \quad (2)$$

where $N_{0,i}$ and b_i are the incoming rates of “good” and “background” decay events [66], and

$$\mathcal{A}_i(t) = \mathcal{A}_{0,i} P_\mu(t), \quad (3)$$

where $\mathcal{A}_{0,i}$ is a proportionality constant typically $\lesssim 0.3$. Note that, written in this manner, Equations (2) and (3) implicitly account for any “instrumental” differences between individual detectors, with the $P_\mu(t)$ treated as common among them.

Following implantation, the μ^+ spins reorient in their local magnetic environment (i.e., at their stopping site). When the local field is transverse to the ensemble's spin direction, $P_\mu(t)$ will precess at a rate equal to the probe's Larmor frequency ω_μ . In the experiments performed here, a so-called transverse-field geometry was used (see, e.g., [7, 11]), wherein an external field $B_{\text{applied}} \approx 10$ mT is applied perpendicular to $P_\mu(t)$'s initial direction (see Figure 1). In this configuration, as mentioned in Section I, only μ^+ in diamagnetic environments contribute to the observable signal, with the paramagnetic “Mu” fraction de-phasing before the earliest time bins [67]. Consequently, at the temperature of the present measurements, the temporal evolution of spin-polarization follows [68]:

$$P_\mu(t) \approx \exp(-\lambda t) \cos(\omega_\mu t + \phi_i), \quad (4)$$

where λ is the damping rate proportional to the width of the (Lorentzian) field distribution, and ϕ_i is a detector-dependent phase factor.

C. Implantation Simulations

Treating μ^+ as a light p^+ , we simulate its implantation into our films using the BCA Monte Carlo code TRIM.SP [27–29]. The simulation inputs (e.g., projectile energy spread, projectile-target atom interaction potential, etc.) were tuned for PSI's LE- μ SR setup (see Section II B), with a thorough account of these details given elsewhere [13, 45]. Crucial to accurate μ^+ range estimation, these simulations make use of the empirical Varelas-Biersack [50] parameterization of electronic stopping cross sections \tilde{S}_e , with values for different (elemental) targets tabulated in the literature [31, 32]. As part of this work, we consider the validity of these compilations using stopping power data available from the IAEA's database [34, 35] (see

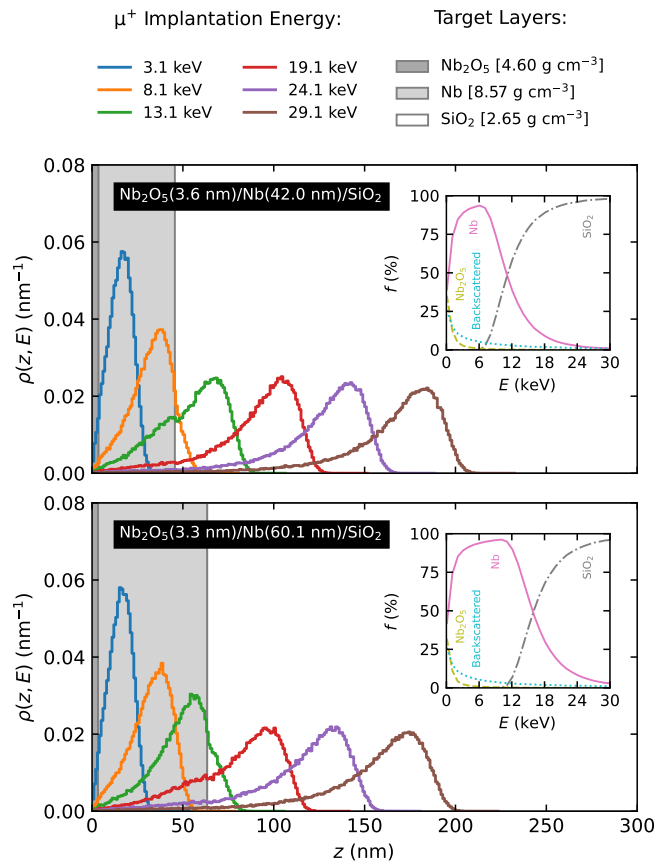


FIG. 2. Typical stopping profiles $\rho(z, E)$ for μ^+ implanted in $\text{Nb}_2\text{O}_5(x \text{ nm})/\text{Nb}(y \text{ nm})/\text{SiO}_2$ [$x = 3.6 \text{ nm}, 3.3 \text{ nm}$; $y = 42.0 \text{ nm}, 60.1 \text{ nm}$] targets at different energies $E \leq 30$ keV. The profiles were simulated using the BCA Monte Carlo code TRIM.SP [27–29] for 10^5 projectiles, with the results represented as histograms with 2 nm bins. Note that these simulations make use of our revised Varelas-Biersack [50] parameterization of each target atom's electronic stopping cross section (see Appendix B). The evolution of the μ^+ stopping fraction f with E is shown in each plot's inset. Further simulation details are described in Section IIC and Refs. [13, 45].

Appendix B). From new Varelas-Biersack [50] fits to the \tilde{S}_e data, we determine improved parameterizations for all target elements considered here (i.e., O, Si, and Nb), with the most consequential updates being for Nb (see Ref. [45]). Further details are given in Appendix B. Using these values, along with those in the older tabulations [31, 32] for comparison, we simulated μ^+ implantation into the Nb/SiO₂/Si films at different E , using 10^5 projectiles in each case. Typical stopping profiles are shown in Figure 2.

III. RESULTS

Typical time-differential LE- μ SR data in the Nb/SiO₂ films at different E are shown in Figure 3. Coherent spin-precession is observed at all measurement conditions, as evidenced by the weakly damped oscillations in $\mathcal{A}_i(t)$. The most striking changes

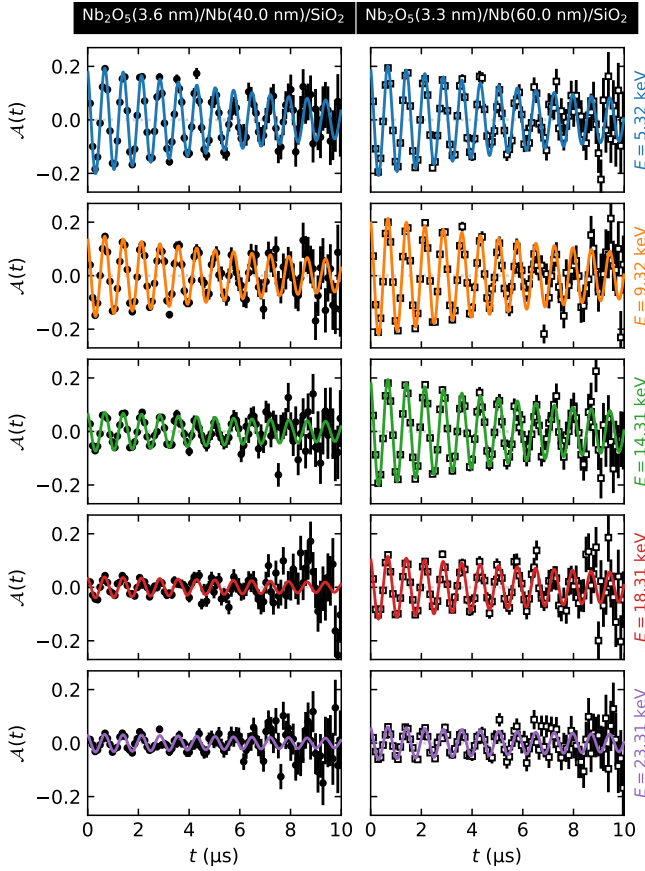


FIG. 3. Typical time-differential LE- μ SR data in the $\text{Nb}_2\text{O}_5(x \text{ nm})/\text{Nb}(y \text{ nm})/\text{SiO}_2$ [$x = 3.6 \text{ nm}, 3.3 \text{ nm}$; $y = 42.0 \text{ nm}, 60.1 \text{ nm}$] films measured at $T = 200 \text{ K}$ in a $B_{\text{applied}} = 10 \text{ mT}$ transverse-field at different implantation energies E and a μ^+ transport bias $\text{Tr} = 15 \text{ keV}$. Note that only the signal in one of four detectors (binned by a factor of 500) is shown for clarity. The solid colored lines denote fits to Equations (2) to (4), in excellent agreement with the data. The amplitude $\mathcal{A}(t = 0 \mu\text{s}) \equiv \mathcal{A}_0$ of the observable single is proportional to the population of implanted μ^+ in a diamagnetic state, corresponding (predominantly) to μ^+ stopped in the Nb layer, which decreases with increasing E .

to the data is the loss in signal amplitude $\mathcal{A}_i(t = 0 \mu\text{s}) \equiv \mathcal{A}_{0,i}$ with increasing E , corresponding to more μ^+ stopping in SiO_2 where the diamagnetic fraction f_{dia} is small (see Figures 1 and 2). The E where the decrease in $\mathcal{A}_{0,i}$ onsets is different for the two films, reflecting the differing thickness of their Nb layers. To quantify these changes, we fit the data to Equations (1) to (4) using `musrfit` [69], yielding excellent agreement with the data (typical reduced negative log-likelihood $\tilde{\mathcal{L}} \approx 1.01$ for each fit.). The E -dependence of the main fit parameters extracted from this procedure are shown in Figure 4 and we consider them in detail below.

First we consider the $\mathcal{A}_{0,i}$ s. Mirroring the changes in signal amplitude with E shown in Figure 3, the $\mathcal{A}_{0,i}$ s in both films decrease when $E \gtrsim 10 \text{ keV}$. At lower E , a film-dependent maximum is reached, whereafter $\mathcal{A}_{0,i}$ decreases with decreasing E , reflecting, for example, the increased probability of μ^+ backscattering off the sample target [13, 70]. The

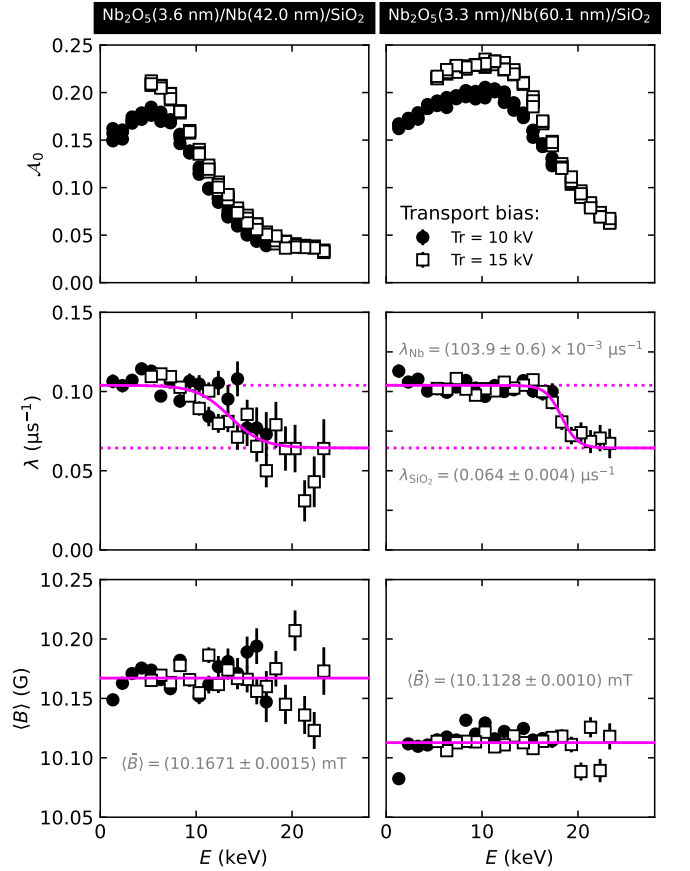


FIG. 4. Implantation energy E dependence of the main fit parameters derived from the analysis of the LE- μ SR data in the $\text{Nb}_2\text{O}_5(x \text{ nm})/\text{Nb}(y \text{ nm})/\text{SiO}_2$ [$x = 3.6 \text{ nm}, 3.3 \text{ nm}$; $y = 42.0 \text{ nm}, 60.1 \text{ nm}$] films at $T = 200 \text{ K}$ in a $B_{\text{applied}} = 10 \text{ mT}$ transverse-field using Equations (2) to (4). Here, \mathcal{A}_0 is the initial asymmetry, proportional to the population of μ^+ stopped in a diamagnetic environment, λ is the exponential damping rate, and $\langle B \rangle$ is the mean local field experienced by the spin-probes. While systematic differences are evident for the \mathcal{A}_0 s determined at different transport biases Tr (e.g., due to slightly different initial spin states), their E -dependence is identical up to a normalization factor. The sigmoidal E -dependence of λ reflects the different damping rates for the Nb and SiO_2 layers, whose asymptotic values (λ_{Nb} and λ_{SiO_2}) are given in the plot inset. Values for the E -independent local field values $\langle B \rangle$ are also indicated.

intrinsic nature of these trends is confirmed by measurements using a different μ^+ transport bias Tr , which show the same E -dependence. We note, however, that there is a small offset between the data acquired using $\text{Tr} = 10 \text{ keV}$ and 15 keV . This difference is *instrumental*, reflecting, for example, slightly different initial polarizations of the μ^+ beam for the two Tr values, and is easily rectified by a “normalization” factor on the order of unity. Importantly, this detail does not impact the extraction of f_{dia} from either dataset (see below).

Next we consider the depolarization rate λ , whose main feature is a sigmoidal E -dependence, gradually transitioning from a value of $\sim 0.11 \mu\text{s}^{-1}$ to $\sim 0.07 \mu\text{s}^{-1}$. We interpret this change as reflecting differences in the local field distribution inside the Nb and SiO_2 layers, with measurements at low (high)

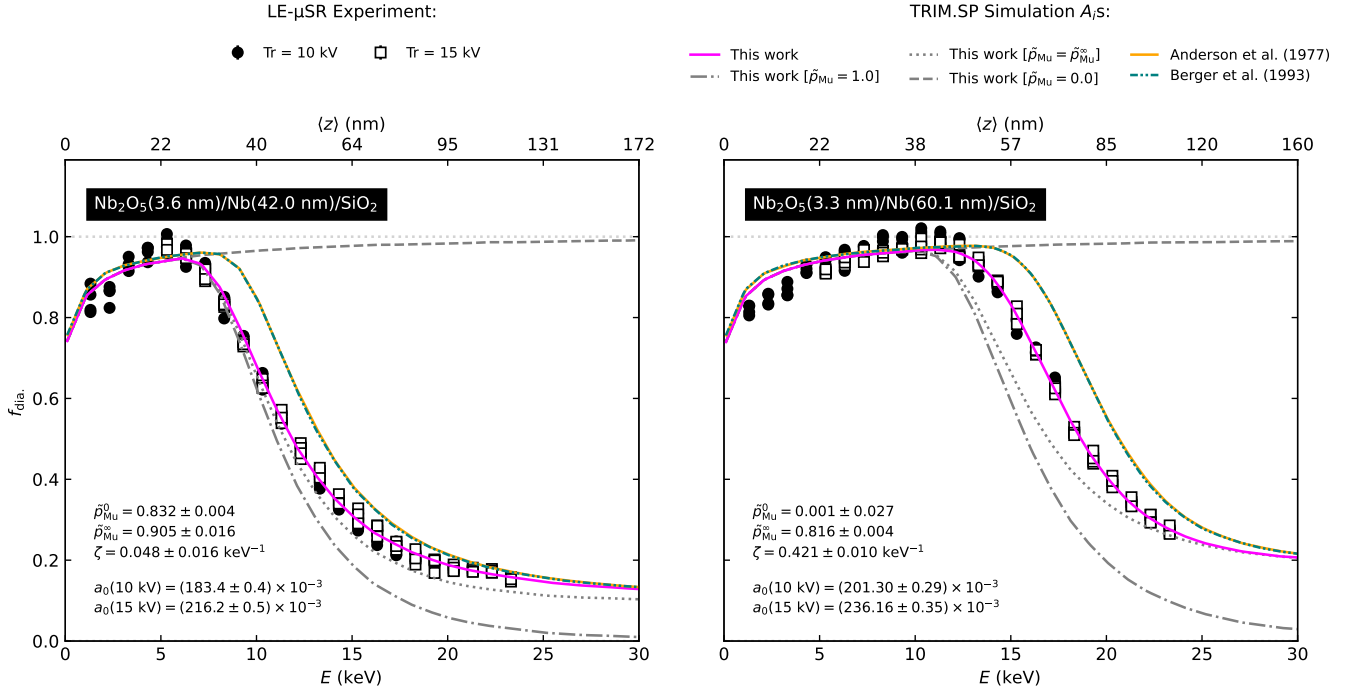


FIG. 5. Measured diamagnetic fraction $f_{\text{dia.}}$ as a function of μ^+ implantation energy E in the $\text{Nb}_2\text{O}_5(x \text{ nm})/\text{Nb}(y \text{ nm})/\text{SiO}_2$ [$x = 3.6 \text{ nm}, 3.3 \text{ nm}$; $y = 42.0 \text{ nm}, 60.1 \text{ nm}$] thin films at $T = 200 \text{ K}$ in a transverse applied field $B_{\text{applied}} \approx 10 \text{ mT}$. Data points correspond to measurements by LE- μSR using two different μ^+ beam extraction biases Tr . The lines indicate predictions by the BCA Monte Carlo code TRIM.SP [27–29] using different muonium formation probabilities $\tilde{p}_{\text{Mu}}(E^*)$ and electronic stopping cross section parameterizations. Simulations using revised inputs derived from the IAEA’s stopping parameters [34, 35] (extending the work in Ref. [45]) are in excellent agreement with the data, in contrast to predictions based on older cross section tabulations [31, 32], which systematically underestimate the range of μ^+ (i.e., predict larger $f_{\text{dia.}}$ s). Note that the $f_{\text{dia.}}$ s simulated using the older tabulations [31, 32] are nearly indistinguishable, owing to their similar stopping coefficients A_i for O, Si, and Nb (see Table II).

E s predominantly sampling the Nb (SiO_2) layers. Using a phenomenological model to describe this partitioning, from its asymptotic limits we determine $\lambda_{\text{Nb}} = 0.1039(6) \mu\text{s}^{-1}$ and $\lambda_{\text{SiO}_2} = 0.064(4) \mu\text{s}^{-1}$. Noting that the intrinsic local field distribution in Nb is Gaussian, characterized by a damping parameter $\sim 0.5 \mu\text{s}^{-1}$ (see, e.g., [71–73]), the observed exponential damping and small λ_{Nb} indicate that μ^+ is mobile at 200 K; however, its finite value suggests the absence of complete “motional narrowing” (cf. [74]). While significant μ^+ motion can complicate implantation studies, site-to-site “hopping” rates $\nu \gtrsim 10^9 \text{ s}^{-1}$ are required to appreciably affect $\mathcal{A}_{0,i}$ [13]. We assert that the modest μ^+ mobility at 200 K [74, 75] is insufficient to be of detriment to our implantation studies. We shall revisit this point later in Section IV.

Before proceeding, we briefly touch upon the B s extracted from our fits to the LE- μSR data. Though some small scatter is evident (e.g., at high E where the signal is small), consistent with expectations for a nonmagnetic heterostructure, B is found to be E -independent. Note that the minor difference in the average values $\langle B \rangle$ determined for both samples (see the inset in Figure 4) reflects their slightly different geometries, amounting to different demagnetization contributions to B (see, e.g., [9]).

With the main fit results outlined above, we now evaluate the E -dependence of the $\mathcal{A}_{0,i}$ s in Figure 4 and convert them to $f_{\text{dia.}}$ s using results from the TRIM.SP [27–29] simulations

of μ^+ implantation (described in Section II C). From the μ^+ stopping fractions in Figure 2, $f_{\text{dia.}}$ may be calculated as [13]:

$$f_{\text{dia.}}(E) \approx f_{\text{Nb}_2\text{O}_5}(E) + f_{\text{Nb}}(E) + [1 - \tilde{p}_{\text{Mu}}(E^*)] f_{\text{SiO}_2}(E), \quad (5)$$

where $f_i(E) \in [0, 1]$ is the fraction of μ^+ stopped in layer $i = \{\text{Nb}_2\text{O}_5, \text{Nb}, \text{SiO}_2\}$ (the signal in Nb_2O_5 is assumed to be purely diamagnetic [76]), and $\tilde{p}_{\text{Mu}}(E^*)$ is the Mu formation probability in SiO_2 . This latter quantity is known to be E -dependent, decreasing from its “bulk” value as $E \rightarrow 0 \text{ keV}$ [13, 58, 59]. We account for this detail explicitly using the mean energy E^* of μ^+ transmitted through the $\text{Nb}_2\text{O}_5/\text{Nb}$ layers [77]:

$$\tilde{p}_{\text{Mu}}(E^*) \approx \left(\tilde{p}_{\text{Mu}}^0 - \tilde{p}_{\text{Mu}}^\infty \right) \exp(-\zeta E^*) + \tilde{p}_{\text{Mu}}^\infty, \quad (6)$$

where $\tilde{p}_{\text{Mu}}^\infty$ is the Mu formation probability in the high- E^* limit, \tilde{p}_{Mu}^0 is the formation probability for $E^* \rightarrow 0 \text{ keV}$, and ζ is a constant defining the interpolation between the two limits. Note that while the form of Equation (6) is phenomenological, it is consistent with the (limited) data on E -dependent Mu formation (see, e.g., [13, 58, 59]). The diamagnetic fraction is related to the observed $\mathcal{A}_{0,s}$ by:

$$\mathcal{A}_0(E, \text{Tr}) = a_0(\text{Tr}) f_{\text{dia.}}(E), \quad (7)$$

where $a_0(\text{Tr})$ is a scaling factor that depends on transport bias (cf. Figure 4).

To identify the $a_0(\text{Tr})$ s and the parameterization of $\tilde{p}_{\text{Mu}}(E^*)$, for each sample the $\mathcal{A}_{0,i}$ s at each Tr were fit with Equations (5) to (7). This was done for implantation simulations using our revised Varelas-Biersack [50] fit of the \tilde{S}_e data for each element in our films (see Appendix B), as well as values from older tabulations [31, 32]. The fit results are shown in Figure 5, with the resulting fit parameters given in the inset. The best agreement is obtained for simulations using our revised fit to the target element \tilde{S}_e s. Interestingly, \tilde{p}_{Mu} 's E -dependence turned out to be somewhat different for the two films; however, we note that both of their high- E limiting values are in good agreement with the range expected for keV implantation energies [13, 58–60]. We shall consider this further in the subsequent section.

IV. DISCUSSION

It is clear from Figure 5 that our revised \tilde{S}_e coefficients give the best agreement with the LE- μ SR data. For $E \gtrsim 5$ keV, the f_{dia} , derived from the TRIM.SP [27–29] implantation simulations closely follows the LE- μ SR measurements, accurately accounting for the partitioning of μ^+ across the Nb and SiO₂ layers. In contrast, the simulations relying on older \tilde{S}_e tabulations [31, 32] systematically overestimate f_{dia} on the high E side of its maximum. This is (predominantly) a consequence of Nb's electronic stopping cross section being overestimated near its maximum in older tabulations [31, 32], which was pointed out previously [45]. These measurements highlight the importance of having high-quality stopping data publicly available [34, 35] and judiciously inspecting the details of the stopping profile simulations used to complement a LE- μ SR experiment.

As mentioned in Section III, one of the “degrees of freedom” in our implantation profile modeling is the muonium formation probability $\tilde{p}_{\text{Mu}}(E^*)$ in SiO₂, which warrants further inspection. In “bulk” μ SR where μ^+ is implanted at ~ 4.1 MeV, \tilde{p}_{Mu} is close to unity, with only a small ~ 15 % fraction of μ^+ remaining in a diamagnetic state in the insulating oxide [13, 57–60]. This remains constant until the μ^+ implantation energy is lowered to $\lesssim 10$ keV, whereafter f_{dia} increases exponentially with decreasing E . This behavior reflects the onset of Mu's delayed formation [78] once sufficient “excess” electrons e^- become available from μ^+ 's ionization track (based on SiO₂'s electron-hole pair creation energy of ~ 18 eV [79], this corresponds to roughly $\sim 1000 e^-$ [59]). Qualitatively, this is similar to what we observe in Figure 5, where the important quantity is the energy E^* of μ^+ transmitted through the Nb₂O₅/Nb layers (see Appendix C), which is akin to a reduced E . While \tilde{p}_{Mu} 's E -dependence is known to be sample-dependent (see, e.g., [13, 58, 59]), it is surprising that the $\tilde{p}_{\text{Mu}}(E^*)$ details differ for our two films, particularly in the low- E^* range (see Figure 6). To explain this observation, we consider the impact of μ^+ energy straggling in our films.

Energy straggling is the variation in projectile energy following traversal through a target (i.e., $E^* \pm \delta E^*$), arising from the stochastic nature of ion-implantation. This effect is already integral to LE- μ SR, accounting for E 's ~ 450 eV distribution “width” from passage through a thin carbon-foil “trigger” prior

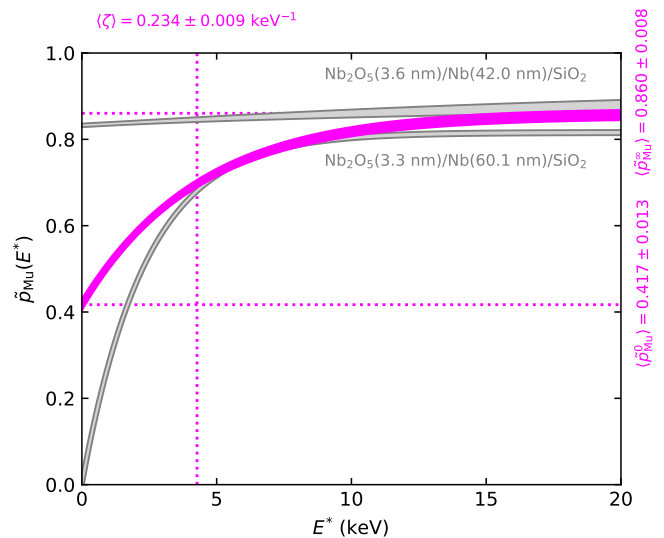


FIG. 6. Muonium formation probability \tilde{p}_{Mu} as a function of the mean energy E^* of μ^+ transmitted through the Nb₂O₅/Nb layers. The shaded grey “bands” denote the ~ 68 % confidence region for each film’s $\tilde{p}_{\text{Mu}}(E^*)$, as given by Equation (6) and the best-fit parameters listed in Figure 5’s inset. The magenta “band” shows a similar confidence region for both film’s average, which is characterized by the parameters in angular brackets $\langle \dots \rangle$ annotating the curve. The average behavior is in good accord with \tilde{p}_{Mu} 's E -dependence in SiO₂ samples [13, 58, 59].

to implantation [80], and is similar to range straggling, producing the spread in μ^+ 's stopping profiles (see Figure 2). As the degree of straggling grows with the amount of material a projectile passes through, we expect it to be largest in our thickest film, a detail confirmed by simulations (see Appendix C). We notice that, once μ^+ starts to penetrate into the insulating layer, E^* remains small (i.e., < 1 keV) over a wider range of E for the thicker film. We suggest that this detail, in conjunction with the larger energy straggling, likely means that the low-energy tail of transmitted energy distribution is poorly encapsulated by E^* . This is consistent with the smaller \tilde{p}_{Mu} observed for the thicker film, which is equivalent to a higher weighting of lower “effective” transmission energies.

Alternatively, it may simply be that the differences observed in $\tilde{p}_{\text{Mu}}(E^*)$ are intrinsic to each film. As mentioned above, the muonium formation probability is known to vary somewhat depending on the SiO₂ sample (see, e.g., [13, 57–60]). In the high- E limit, our $\tilde{p}_{\text{Mu}}^{\infty}$ s agree nicely with the expected range of variation for the insulator, so the differences are isolated to low E^* . While it is difficult to be conclusive about their origin, we point out that the *average* behavior $\langle \tilde{p} \rangle(E^*)$ is in good accord with the E -dependence from other measurements in SiO₂ [13, 58, 59]. Thus, the overall behavior is consistent with what is known about μ^+ in the insulating layer. In the future, it may be interesting to explore this energy-dependence across a variety sample sources.

One important aspect not considered in detail thus far is the impact of μ^+ diffusion in Nb (see Section III). While μ^+ can be viewed chemically as a *very* light proton (see, e.g., [10]),

its small mass makes it much more amenable to translational motion, leading to substantial mobility in many metals [81], even at cryogenic temperatures [82]. Nb is no exception, with the exponential decay of $P_\mu(t)$ implying μ^+ 's mobility at 200 K. In the static limit, $P_\mu(t)$'s envelope is expected to be Gaussian, reflecting a normal distribution of fields at the stopping site. Quite generally, when the local field is altered by a stochastic process (e.g., thermally activated site-to-site probe “hopping”), the field distribution is dynamically modified. When the rate ν of the dynamics is sufficiently high (i.e., $\nu \gtrsim \omega_\mu$), dynamic averaging causes the field distribution to “narrow” to a Lorentzian, yielding an exponential envelope with a decay constant given by (see, e.g., [9]):

$$\lambda = \frac{\sigma^2}{\nu} \left(1 + \frac{1}{1 + (\omega_\mu/\nu)^2} \right), \quad (8)$$

where σ is the (static-limit) Gaussian damping rate. Noting the small E -dependence to λ in Figure 4 (i.e., from different values in the Nb and SiO₂ layers), we take Nb's measured asymptotic value $\lambda_{\text{Nb}} = 0.1039(6) \mu\text{s}^{-1}$, along with $\sigma \approx 0.50(2) \mu\text{s}^{-1}$ (see, e.g., [71–73]) and $\omega_\mu = 8.6585(13) \mu\text{s}^{-1}$, which from Equation (8) yield $\nu = 2.61(24) \mu\text{s}^{-1}$ [83]. This is much less than the $\nu \gtrsim 10^9 \text{ s}^{-1}$ criteria [13] needed to appreciably influence the $A_{0,i}$ s reported in Figure 4. For comparison, if we assume that μ^+ migration takes place via high-symmetry interstitial sites (e.g., the “octahedral” or “tetrahedral” positions) [84], this corresponds to a diffusion length on the order of $\sim 0.5 \text{ nm}$ over μ^+ 's lifetime, which is negligible. Therefore, we reiterate the assertion made in Section III that this modest mobility is insufficient to be of detriment to the implantation measurements.

Having considered the details of our stopping profile comparisons, we conclude this section with a brief discussion of the impact of our results. In order to accurately track the length scales probed by LE- μ SR, it is essential that the stopping simulations used to complement the experimental work provide reliable estimates for μ^+ 's range. This need is even more imperative when depth-resolved information are at the heart of the physics under investigation (e.g., the length scales associated with a superconducting state [45, 48]). This accuracy has been confirmed for many “noble” metals [13, 33] commonly used, for example, as substrates, spacers, or capping layers in condensed matter research; however, the available stopping cross section data [34, 35] suggest this agreement is less established across the periodic table. The present case of Nb is exemplary of this point, with earlier measurements having likely underestimated its superconducting length scales (e.g., its magnetic penetration depth) [42, 44, 73]. In the future, it would be interesting to perform similar experiments to those described herein on other elemental metals where stopping data is either sparse (e.g., Na, Ru, or Eu) or absent (e.g., Ho, Rh, or Pr) [34, 35]. Such an undertaking may prove challenging in rare-earth metals due to their strong electronic moments, which may be magnetically ordered. In the intervening time before such experimental verifications are made, leveraging the available stopping data and applying contemporary predictive techniques (see, e.g., [36–39]) may be the best approach for ensuring accurate depth-resolution with LE- μ SR.

V. CONCLUSIONS

Using LE- μ SR, we studied the range of $E = 1.3 \text{ keV}$ to 23.3 keV implanted μ^+ in Nb₂O₅($x \text{ nm}$)/Nb($y \text{ nm}$)/SiO₂ [$x = 3.6 \text{ nm}, 3.3 \text{ nm}; y = 42.0 \text{ nm}, 60.1 \text{ nm}$] films using the observed μ^+ fraction stopped in a diamagnetic environment. Using the Monte Carlo code TRIM.SP [27–29], treating μ^+ as a light p^+ with simulation inputs tuned for LE- μ SR [13], we compared the measured fractions against predictions using our revised and older tabulations [31, 32] of p^+ stopping powers in Nb. In conjunction with a model for μ^+ 's E -dependent formation probability, we find that revised stopping coefficients yield predictions in excellent agreement with the LE- μ SR measurement, while the older tabulations [31, 32] underestimate μ^+ 's range in Nb. Our results indicate that earlier experiments — with a few exceptions [45, 85] — relying on knowledge of the μ^+ stopping profile in Nb or Nb compounds (e.g., measurements of the Meissner screening profile) likely underestimate the lengths derived in their work. In the future, it would be interesting to perform similar tests on other elements in the stopping power database [34, 35], especially those where low-energy data is sparse or absent.

ACKNOWLEDGMENTS

T. Junginger acknowledges financial support from NSERC. This work is based on experiments performed at the S μ S, PSI, Villigen, Switzerland (proposal number 20230035).

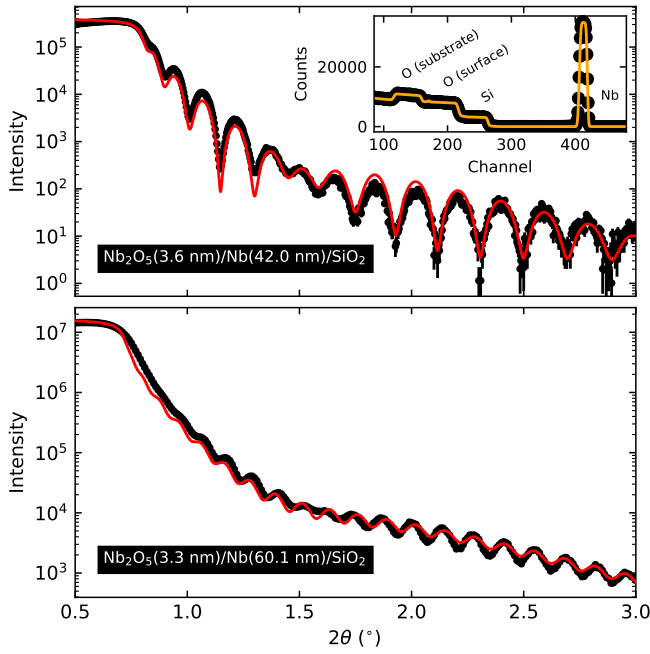


FIG. 7. XRR measurements of the two Nb films. The solid red lines are fits to the data, with the corresponding layer thicknesses indicated in each subplot and Table I. As an independent check, RBS measurements on the thinner film were also performed (data and SIMNRA [87] simulation shown in the inset), yielding thickness estimates in good agreement with XRR (see Table I).

TABLE I. Summary of the layer thickness measurements using XRR and RBS for the two $\text{Nb}_2\text{O}_5(x \text{ nm})/\text{Nb}(y \text{ nm})/\text{SiO}_2(300 \text{ nm})/\text{Si}$ films.

| Sample | x (nm) | y (nm) | Method |
|--------|----------|----------|--------|
| Thin | 3.6 | 42.0 | XRR |
| | 3.6(4) | 45.5(23) | RBS |
| Thick | 3.3 | 60.1 | XRR |

Appendix A: Film Thickness characterization

As mentioned in Section II A, the thickness of each Nb film was confirmed using XRR. Reflectivity spectra in both films and a fit to the data are shown in Figure 7, with the corresponding layer thicknesses tabulated in Table I. As an independent check, RBS measurements (2 MeV $^4\text{He}^+$ beam with a scattering angle of 167.5° and a 30° tilt) were performed on one of the films (see Figure 7), yielding thickness estimates in good agreement with XRR (see Table I). Elastic recoil detection analysis (ERDA) measurements (ToF-E spectrometer with 13 MeV ^{127}I under a total scattering angle of 36° [86]) were also performed on this film, confirming the absence of contamination by light elements (e.g., H, C, and N).

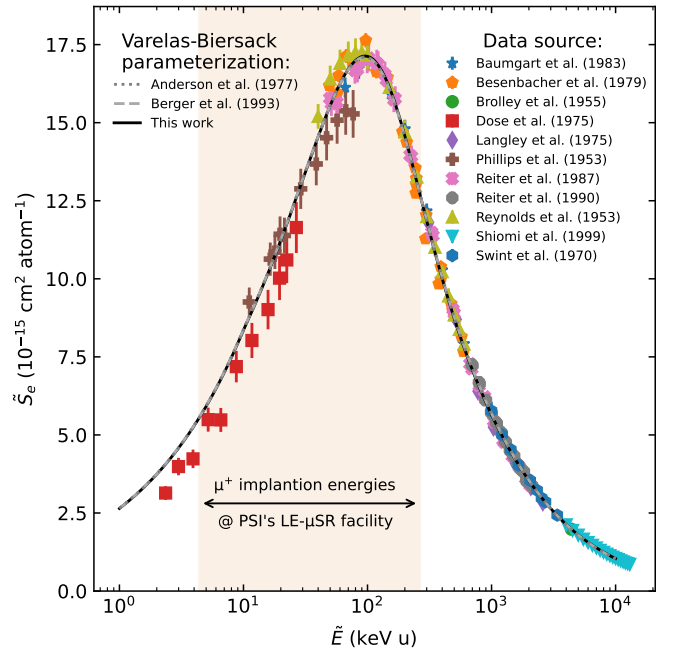


FIG. 8. Measured electronic stopping cross sections \tilde{S}_e for proton-like projectiles implanted in O_2 at different scaled energies \tilde{E} . The coloured points denote results from all available studies [88–98]. Several Varel-Biersack [50] parameterizations are shown [31, 32] along with our own fit, each in good agreement with the data. The data were curated by the IAEA as part of their electronic stopping database [34, 35].

Appendix B: Electronic Stopping Cross Sections

Critical to accurate projectile range estimation from ion-implantation simulation codes, such as the BCA Monte Carlo application TRIM.SP [27–29] used here (see Section II C), is the handling of the electronic contribution to the target material’s total stopping power. For proton-like projectiles (e.g., μ^+), this (inelastic) energy dissipation can be treated empirically using the Varel-Biersack expressions [50], which parameterize an elemental target’s electronic stopping cross sections \tilde{S}_e , in terms of five coefficients A_i ($i \in \{1, 2, 3, 4, 5\}$) that cover the “low-energy” implantation region near \tilde{S}_e ’s maximum. the E -dependence is expressed in terms of the scaled quantity:

$$\tilde{E} \equiv E \left(\frac{u}{m} \right), \quad (\text{B1})$$

where m is the projectile’s mass and u is the atomic mass unit [1, 32], the latter ensuring both E and \tilde{E} are dimensionally equivalent (cf. [31]). Explicitly, \tilde{S}_e is given by [31, 32, 50]:

$$\tilde{S}_e = \begin{cases} A_1 \sqrt{\tilde{E}}, & \tilde{E} \leq 10 \text{ keV}, \\ \frac{s_{\text{low}}(\tilde{E}) s_{\text{high}}(\tilde{E})}{s_{\text{low}}(\tilde{E}) + s_{\text{high}}(\tilde{E})}, & \tilde{E} > 10 \text{ keV}, \end{cases} \quad (\text{B2})$$

where

$$s_{\text{low}}(\tilde{E}) = A_2 \tilde{E}^{0.45}, \quad (\text{B3})$$

TABLE II. Values for the (empirical) Varelas-Biersack [50] coefficients A_i in Equations (B2) to (B4) parameterizing the electronic stopping cross section \tilde{S}_e for proton-like projectiles in different elemental targets. Note that $\text{SU} \equiv 10^{-15} \text{ eV cm}^2 \text{ atom}^{-1}$ has been used when defining the units for some of the A_i 's.

| Target | A_1 (SU $\text{keV}^{-1/2}$) | A_2 (SU $\text{keV}^{-0.45}$) | A_3 (SU keV) | A_4 (keV) | A_5 (keV^{-1}) | Ref. |
|--------------|---------------------------------|----------------------------------|----------------|-------------|-----------------------------|-----------|
| O_2 | 2.652 | 3 | 1920 | 2000 | 0.0223 | [31] |
| | 2.652 | 3 | 1920 | 2000 | 0.0223 | [32] |
| | 2.645(14) | 2.992(16) | 1984(16) | 1900(60) | 0.0195(7) | This work |
| Si | 4.15 | 4.7 | 3329 | 550 | 0.013 21 | [31] |
| | 4.914 | 5.598 | 3193 | 232.7 | 0.014 19 | [32] |
| | 4.92(4) | 5.61(5) | 2610(100) | 370(27) | 0.0253(28) | This work |
| Nb | 6.902 | 7.791 | 9333 | 442.7 | 0.005 587 | [31] |
| | 6.901 | 7.791 | 9333 | 442.7 | 0.005 587 | [32] |
| | 5.84(6) | 6.58(7) | 12 600(600) | 206(11) | 0.002 70(24) | This work |

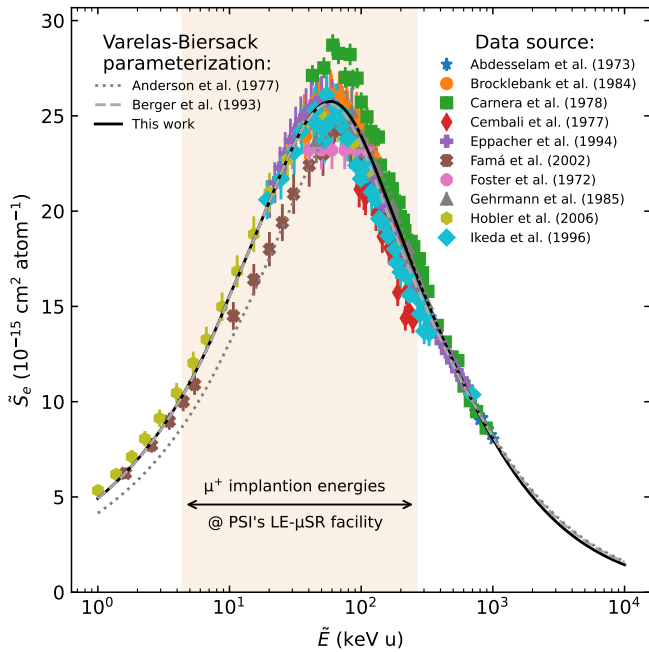


FIG. 9. Measured electronic stopping cross sections \tilde{S}_e for proton-like projectiles implanted in Si at different scaled energies \tilde{E} . The coloured points denote results from all available studies [99–108] (apart from two sets of outliers [109, 110]). Several Varelas-Biersack [50] parameterizations are shown [31, 32] along with our own fit, each in good agreement with the data. The data were curated by the IAEA as part of their electronic stopping database [34, 35].

and

$$s_{\text{high}}(\tilde{E}) = \left(\frac{A_3}{\tilde{E}} \right) \ln \left(1 + \frac{A_4}{\tilde{E}} + A_5 \tilde{E} \right). \quad (\text{B4})$$

While these expressions are not unique (see, e.g., [26]), they provide an excellent description of \tilde{S}_e 's \tilde{E} -dependence in most elements. For compound targets, Bragg's additivity rule [111] is used, which remains a reasonable approximation at low \tilde{E} [35].

While the qualitative form of Equations (B2) to (B4) is known to be correct, their accuracy depends on the A_i 's used, with

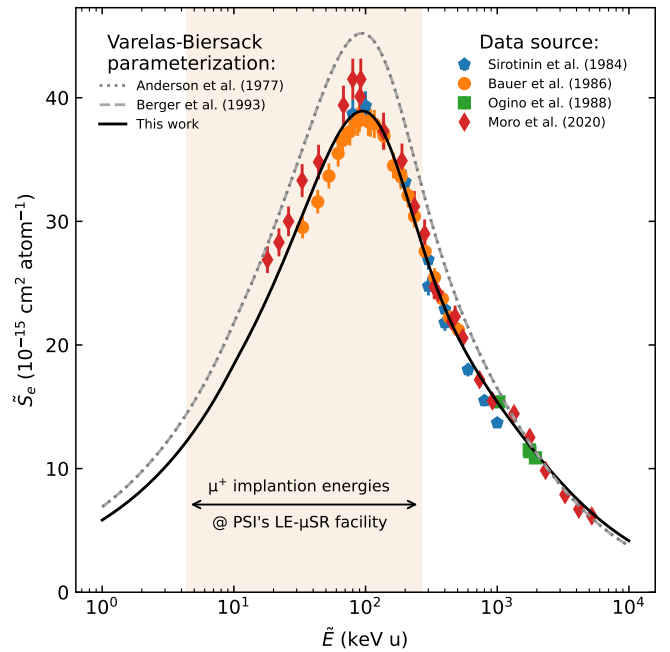


FIG. 10. Measured electronic stopping cross sections \tilde{S}_e for proton-like projectiles implanted in Nb at different scaled energies \tilde{E} . The coloured points denote results from all available studies [51–54] (apart from one set of outliers [55]). Several Varelas-Biersack [50] parameterizations are shown [31, 32] along with our own fit, which supersedes our previous parameterization (see Ref. [45]). While our revised fit is in excellent agreement with the data, the older tabulations [31, 32], overestimate \tilde{S}_e near the peak maximum. The data were curated by the IAEA as part of their electronic stopping database [34, 35].

tabulations for target elements up to uranium available [31, 32]. Recently, the validity of these values for Nb was considered [45], with data from the IAEA's electronic stopping power database (version 2021-12) [34, 35] showing that the tabulations [31, 32] overestimate \tilde{S}_e around its maximum. Here, we expand on this assessment using the database's latest version (2024-03) [34, 35] and include additional elemental targets.

Figures 8 to 10 show measured \tilde{S}_e 's for proton-like projectiles

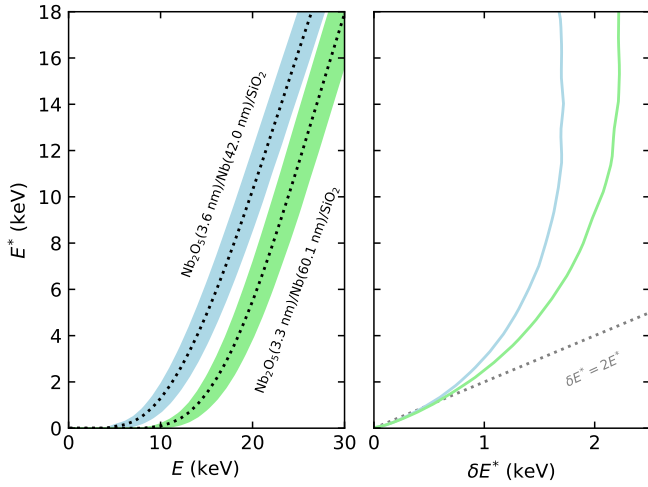


FIG. 11. Mean energy E^* of μ^+ transmitted through the $\text{Nb}_2\text{O}_5/\text{Nb}$ layers as a function of implantation energy E , obtained from TRIM.SP [27–29] simulations without the SiO_2 substrate. The shaded colored regions denote the span of $E^* \pm \delta E^*$ (its standard deviation). The relationship between E^* and δE^* is also shown. In these simulations, we have used the Varelas-Biersack [50] coefficients derived in this work as inputs (see Table II).

implanted in O_2 [88–98], Si [99–108], and Nb [51–54] targets. Note that measurements which are clear outliers (Refs. [109, 110] for Si and Ref. [55] for Nb) have been omitted. For each target’s data, we fit the \tilde{E} -dependence using the Varelas-Biersack expressions [50], with the result shown as a solid black line. In doing this, we followed the approach in Ref. [45], where it was pointed out that the smooth continuity of Equation (B2) implies that:

$$A_1 \equiv \left(\frac{1}{\sqrt{10 \text{ keV}}} \right) \frac{s_{\text{low}}(10 \text{ keV}) s_{\text{high}}(10 \text{ keV})}{s_{\text{low}}(10 \text{ keV}) + s_{\text{high}}(10 \text{ keV})},$$

reducing the number fitted A_i s from five to four. This choice is most consequential for fitting the \tilde{S}_e data in Nb (see Figure 10),

where measurements in the region $\tilde{E} \lesssim 10 \text{ keV}$ are absent. For O_2 (see Figure 8) and Si (see Figure 9), this constraint is not detrimental to the fit, as evidenced by the good agreement with the data in this \tilde{E} -region. For comparison, $\tilde{S}_e(\tilde{E})$ curves using literature A_i s [31, 32] are also shown in Figures 8 to 10. In each case, our fit gives the best agreement with the \tilde{S}_e data. Explicit values for our newly determined A_i s, along with values for the older tabulations [31, 32], are given in Table II. Note that the values reported in Table II for Nb supersede those in Ref. [45], which were derived from an earlier version (2021-12) of the IAEA’s database [34, 35] that did not explicitly include uncertainty estimates.

Appendix C: μ^+ Transmission through $\text{Nb}_2\text{O}_5/\text{Nb}$

In the model introduced in Section III to account for Mu’s energy-dependent formation probability [Equation (6)], one of its dependencies is the mean energy E^* of μ^+ transmitted through the $\text{Nb}_2\text{O}_5/\text{Nb}$ layers. This quantity is not directly available from implantation simulations shown in Figure 2, but may be obtained from separate TRIM.SP [27–29] calculations where the SiO_2 substrate is omitted. The E -dependence of E^* for our two films is shown in Figure 11, where we have used the Varelas-Biersack [50] coefficients derived in this work as inputs (see Table II). While an $E^* \approx 0 \text{ keV}$ indicates insufficient passage into the insulating layer, E^* increases monotonically once E is sufficiently high. Importantly, we point out that encapsulating μ^+ transmission using E^* is an approximation; the energy of muons eluting out of the $\text{Nb}_2\text{O}_5/\text{Nb}$ layers really follow a *distribution* (i.e., due to range straggling). This is emphasized by the shaded colored regions in Figure 11, which denote the span of $E^* \pm$ its standard deviation δE^* . Notice that, particularly for the thicker film, the $E^* \pm \delta E^*$ “band” remains close to zero for a wider E -region than in the thinner film. This detail, in conjunction with the larger δE^* for the thicker film, likely contributes to the different $\tilde{p}_{\text{Mu}}(E^*)$ s observed for the two films at low E^* values (see Figure 6).

-
- [1] E. Tiesinga, P. J. Mohr, D. B. Newell, and B. N. Taylor, CODATA recommended values of the fundamental physical constants: 2018, *Rev. Mod. Phys.* **93**, 025010 (2021).
 - [2] R. L. Workman *et al.* (Particle Data Group), Review of particle physics, *Prog. Theor. Exp. Phys.* **2022**, 083C01 (2022).
 - [3] A. D. Hillier, S. J. Blundell, I. McKenzie, I. Umegaki, L. Shu, J. A. Wright, T. Prokscha, F. Bert, K. Shimomura, A. Berlie, H. Alberto, and I. Watanabe, Muon spin spectroscopy, *Nat. Rev. Methods Primers* **2**, 4 (2022).
 - [4] A. J. Pell, G. Pintacuda, and C. P. Grey, Paramagnetic NMR in solution and the solid state, *Prog. Nucl. Magn. Reson. Spectrosc.* **111**, 1 (2019).
 - [5] J. H. Brewer, Problems and opportunities: The early history of μSR , *Phys. Proc.* **30**, 2 (2012).
 - [6] That is, physical systems that are either prohibitively difficult or impossible to study through more “conventional” means of interrogation.
 - [7] A. Yaouanc and P. Dalmas de Réotier, *Muon Spin Rotation, Relaxation, and Resonance: Applications to Condensed Matter*, International Series of Monographs on Physics, Vol. 147 (Oxford University Press, Oxford, 2011).
 - [8] S. J. Blundell, R. De Renzi, T. Lancaster, and F. L. Pratt, eds., *Muon Spectroscopy: An Introduction* (Oxford University Press, Oxford, 2021).
 - [9] A. Amato and E. Morenzoni, *Introduction to Muon Spin Spectroscopy: Applications to Solid State and Material Sciences*, Lecture Notes in Physics, Vol. 961 (Springer Nature Switzerland AG, Cham, 2024).
 - [10] D. G. Fleming, P. W. Percival, and I. McKenzie, *Muon Spin Spectroscopy: Methods and Applications in Chemistry and Materials Science* (Wiley, Weinheim, 2024).
 - [11] P. Bakule and E. Morenzoni, Generation and applications of slow polarized muons, *Contemp. Phys.* **45**, 203 (2004).

- [12] E. Morenzoni, T. Prokscha, A. Suter, H. Luetkens, and R. Khasanov, Nano-scale thin film investigations with slow polarized muons, *J. Phys.: Condens. Matter* **16**, S4583 (2004).
- [13] E. Morenzoni, H. Glückler, T. Prokscha, R. Khasanov, H. Luetkens, M. Birke, E. M. Forgan, C. Niedermayer, and M. Pleines, Implantation studies of keV positive muons in thin metallic layers, *Nucl. Instrum. Methods Phys. Res., Sect. B* **192**, 254 (2002).
- [14] R. F. Kiefl, G. D. Morris, P. Amaudruz, R. Baartman, J. Behr, J. H. Brewer, J. Chakhalian, S. Daviel, J. Doornbos, S. Dunsiger, S. R. Kretziman, T. Kuo, C. D. P. Levy, R. Müller, M. Olivo, R. Poutissou, G. W. Wight, and A. Zelenski, Complementarity of low-energy spin polarized radioactive nuclei and muons, *Physica B* **289–290**, 640 (2000).
- [15] W. A. MacFarlane, Implanted-ion β NMR: A new probe for nanoscience, *Solid State Nucl. Magn. Reson.* **68–69**, 1 (2015).
- [16] W. A. MacFarlane, Status and progress of ion-implanted β NMR at TRIUMF, *Z. Phys. Chem.* **236**, 757 (2022).
- [17] C. Niedermayer, E. M. Forgan, H. Glückler, A. Hofer, E. Morenzoni, M. Pleines, T. Prokscha, T. M. Riseman, M. Birke, T. J. Jackson, J. Litterst, M. W. Long, H. Luetkens, A. Schatz, and G. Schatz, Direct observation of a flux line lattice field distribution across an $\text{YBa}_2\text{Cu}_3\text{O}_{7-\delta}$ surface by low energy muons, *Phys. Rev. Lett.* **83**, 3932 (1999).
- [18] A. Suter, E. Morenzoni, R. Khasanov, H. Luetkens, T. Prokscha, and N. Garifianov, Direct observation of nonlocal effects in a superconductor, *Phys. Rev. Lett.* **92**, 087001 (2004).
- [19] A. Di Bernardo, Z. Salman, X. L. Wang, M. Amado, M. Egilmez, M. G. Flokstra, A. Suter, S. L. Lee, J. H. Zhao, T. Prokscha, E. Morenzoni, M. G. Blamire, J. Linder, and J. W. A. Robinson, Intrinsic paramagnetic Meissner effect due to s -wave odd-frequency superconductivity, *Phys. Rev. X* **5**, 041021 (2015).
- [20] M. G. Flokstra, N. Satchell, J. Kim, G. Burnell, P. J. Curran, S. J. Bending, J. F. K. Cooper, C. J. Kinane, S. Langridge, A. Isidori, N. Pugach, M. Eschrig, H. Luetkens, A. Suter, T. Prokscha, and S. L. Lee, Remotely induced magnetism in a normal metal using a superconducting spin-valve, *Nat. Phys.* **12**, 57 (2016).
- [21] Q. N. Meier, M. Fechner, T. Nozaki, M. Sashiki, Z. Salman, T. Prokscha, A. Suter, P. Schoenherr, M. Lilienblum, P. Borisov, I. E. Dzyaloshinskii, M. Fiebig, H. Luetkens, and N. A. Spaldin, Search for the magnetic monopole at a magnetoelectric surface, *Phys. Rev. X* **9**, 011011 (2019).
- [22] J. A. Krieger, A. Pertsova, S. R. Giblin, M. Döbeli, T. Prokscha, C. W. Schneider, A. Suter, T. Hesjedal, A. V. Balatsky, and Z. Salman, Proximity-induced odd-frequency superconductivity in a topological insulator, *Phys. Rev. Lett.* **125**, 026802 (2020).
- [23] R. Fittipaldi, R. Hartmann, M. T. Mercaldo, S. Komori, A. Bjørlig, W. Kyung, Y. Yasui, T. Miyoshi, L. A. B. Olde Olthof, C. M. Palomares Garcia, V. Granata, I. Keren, W. Higemoto, A. Suter, T. Prokscha, A. Romano, C. Noce, C. Kim, Y. Maeno, E. Scheer, B. Kalisky, J. W. A. Robinson, M. Cuoco, Z. Salman, A. Vecchione, and A. Di Bernardo, Unveiling unconventional magnetism at the surface of Sr_2RuO_4 , *Nat. Commun.* **12**, 5792 (2021).
- [24] H. Alpern, M. Amundsen, R. Hartmann, N. Sukenik, A. Spuri, S. Yochelis, T. Prokscha, V. Gutkin, Y. Anahory, E. Scheer, J. Linder, Z. Salman, O. Millo, Y. Paltiel, and A. Di Bernardo, Unconventional Meissner screening induced by chiral molecules in a conventional superconductor, *Phys. Rev. Mater.* **5**, 114801 (2021).
- [25] J. Fowlie, M. Hadjimichael, M. M. Martins, D. Li, M. Osada, B. Y. Wang, K. Lee, Y. Lee, Z. Salman, T. Prokscha, J.-M. Triscone, H. Y. Hwang, and A. Suter, Intrinsic magnetism in superconducting infinite-layer nickelates, *Nat. Phys.* **18**, 1043 (2022).
- [26] J. F. Ziegler, J. P. Biersack, and M. D. Ziegler, *SRIM — The Stopping and Range of Ions in Matter*, 7th ed. (SRIM Co., Chester, 2008).
- [27] J. P. Biersack and W. Eckstein, Sputtering studies with the Monte Carlo program TRIM.SP, *Appl. Phys. A* **34**, 73 (1984).
- [28] W. Eckstein, *Computer Simulation of Ion-Solid Interactions*, Springer Series in Materials Science, Vol. 10 (Springer, Berlin, 1991).
- [29] W. Eckstein, Backscattering and sputtering with the Monte-Carlo program TRIM.SP, *Radiat. Eff. Defects Solids* **130–131**, 239 (1994).
- [30] Note that, as discussed in Ref. [13], the use of SRIM [26] should be avoided for simulating the implantation of μ^+ at keV energies.
- [31] H. H. Anderson and J. F. Ziegler, *Hydrogen: Stopping Powers and Ranges in All Elements*, The Stopping and Ranges of Ions in Matter, Vol. 3 (Pergamon Press, New York, 1977).
- [32] M. J. Berger, M. Inokuti, H. H. Andersen, H. Bichsel, D. Powers, S. M. Seltzer, D. Thwaites, and D. E. Watt, *Stopping Powers and Ranges for Protons and Alpha Particles*, ICRU Report, Vol. 49 (International Commission on Radiation Units and Measurements, Bethesda, 1993).
- [33] H. Glückler, E. Morenzoni, T. Prokscha, M. Birke, E. M. Forgan, A. Hofer, T. J. Jackson, J. Litterst, H. Luetkens, C. Niedermayer, M. Pleines, T. M. Riseman, and G. Schatz, Range studies of low-energy muons in a thin Al film, *Physica B* **289–290**, 658 (2000).
- [34] C. C. Montanari and P. Dimitriou, The IAEA stopping power database, following the trends in stopping power of ions in matter, *Nucl. Instrum. Methods Phys. Res., Sect. B* **408**, 50 (2017).
- [35] C. C. Montanari, P. Dimitriou, L. Marian, A. M. P. Mendez, J. P. Peralta, and F. Bivort-Haiek, The IAEA electronic stopping power database: Modernization, review, and analysis of the existing experimental data, *Nucl. Instrum. Methods Phys. Res., Sect. B* **551**, 165336 (2024).
- [36] W. A. Parfitt and R. B. Jackman, Machine learning for the prediction of stopping powers, *Nucl. Instrum. Methods Phys. Res., Sect. B* **478**, 21 (2020).
- [37] F. Bivort Haiek, A. M. P. Mendez, C. C. Montanari, and D. M. Mitnik, ESPNN: A novel electronic stopping power neural-network code built on the IAEA stopping power database. I. atomic targets, *J. Appl. Phys.* **132**, 245103 (2022).
- [38] F. Akbari, S. Taghizadeh, D. Shvydka, N. N. Sperling, and E. I. Parsai, Predicting electronic stopping powers using stacking ensemble machine learning method, *Nucl. Instrum. Methods Phys. Res., Sect. B* **538**, 8 (2023).
- [39] H. Minagawa, T. Tezuka, and H. Tsuchida, Effective combinations of features in predicting the range of incident ions using machine learning, *Nucl. Instrum. Methods Phys. Res., Sect. B* **553**, 165383 (2024).
- [40] T. Junginger, R. Laxdal, W. A. MacFarlane, and A. Suter, SRF material research using muon spin rotation and beta-detected nuclear magnetic resonance, *Front. Electron. Mater.* **4**, 1346235 (2024).
- [41] H. Padamsee, *Superconducting Radiofrequency Technology for Accelerators: State of the Art and Emerging Trends* (Wiley, Weinheim, 2023).
- [42] A. Suter, E. Morenzoni, N. Garifianov, R. Khasanov, E. Kirk, H. Luetkens, T. Prokscha, and M. Horisberger, Observation of nonexponential magnetic penetration profiles in the Meissner state: A manifestation of nonlocal effects in superconductors, *Phys. Rev. B* **72**, 024506 (2005).

- [43] R. M. L. McFadden *et al.*, Nanoscale quantification of superconducting Nb's fundamental length scales, (unpublished).
- [44] A. Romanenko, A. Grassellino, F. Barkov, A. Suter, Z. Salman, and T. Prokscha, Strong Meissner screening change in superconducting radio frequency cavities due to mild baking, *Appl. Phys. Lett.* **104**, 072601 (2014).
- [45] R. M. L. McFadden, M. Asaduzzaman, T. Prokscha, Z. Salman, A. Suter, and T. Junginger, Depth-resolved measurements of the Meissner screening profile in surface-treated Nb, *Phys. Rev. Appl.* **19**, 044018 (2023).
- [46] R. M. L. McFadden, M. Asaduzzaman, and T. Junginger, Comment on "Strong Meissner screening change in superconducting radio frequency cavities due to mild baking" [Appl. Phys. Lett. 104, 072601 (2014)], *Appl. Phys. Lett.* **124**, 086101 (2024).
- [47] R. M. L. McFadden and T. Junginger, Search for inhomogeneous Meissner screening in Nb induced by low-temperature surface treatments, *AIP Adv.* **14**, 095320 (2024).
- [48] M. Asaduzzaman, R. M. L. McFadden, A.-M. Valente-Feliciano, D. R. Beverstock, A. Suter, Z. Salman, T. Prokscha, and T. Junginger, Evidence for current suppression in superconductor-superconductor bilayers, *Supercond. Sci. Technol.* **37**, 025002 (2024).
- [49] B. W. Maxfield and W. L. McLean, Superconducting penetration depth of niobium, *Phys. Rev.* **139**, A1515 (1965).
- [50] C. Varelas and J. Biersack, Reflection of energetic particles from atomic or ionic chains in single crystals, *Nucl. Instrum. Methods* **79**, 213 (1970).
- [51] E. I. Sirotnin, A. F. Tulinov, V. A. Khodyrev, and V. N. Mizgulin, Proton energy loss in solids, *Nucl. Instrum. Methods Phys. Res., Sect. B* **4**, 337 (1984).
- [52] P. Bauer and D. Semrad, Stopping of hydrogen ions in chemically active metal targets, characterized by AES and RBS, *Nucl. Instrum. Methods Phys. Res., Sect. B* **13**, 201 (1986).
- [53] K. Ogino, T. Kiyosawa, and T. Kiuchi, Stopping powers for MeV tritons in solids, *Nucl. Instrum. Methods Phys. Res., Sect. B* **33**, 155 (1988).
- [54] M. V. Moro, P. Bauer, and D. Primetzhofer, Experimental electronic stopping cross section of transition metals for light ions: Systematics around the stopping maximum, *Phys. Rev. A* **102**, 022808 (2020).
- [55] R. Behrisch and B. M. U. Scherzer, Rutherford back-scattering as a tool to determine electronic stopping powers in solids, *Thin Solid Films* **19**, 247 (1973).
- [56] R. M. L. McFadden, M. Asaduzzaman, T. J. Buck, D. L. Cortie, M. H. Dehn, S. R. Dunsiger, R. F. Kiefl, R. E. Laxdal, C. D. P. Levy, W. A. MacFarlane, G. D. Morris, M. R. Pearson, E. Thoeng, and T. Junginger, Depth-resolved measurement of the Meissner screening profile in a niobium thin film from spin-lattice relaxation of the implanted β -emitter ^8Li , *J. Appl. Phys.* **134**, 163902 (2023).
- [57] D. P. Spencer, D. G. Fleming, and J. H. Brewer, Muonium formation in diamond and oxide insulators, *Hyperfine Interact.* **18**, 567 (1984).
- [58] T. Prokscha, E. Morenzoni, N. Garifanov, H. Glückler, R. Khasanov, H. Luetkens, and A. Suter, Muonium formation at keV energies, *Physica B* **326**, 51 (2003).
- [59] T. Prokscha, E. Morenzoni, D. G. Eshchenko, N. Garifanov, H. Glückler, R. Khasanov, H. Luetkens, and A. Suter, Formation of hydrogen impurity states in silicon and insulators at low implantation energies, *Phys. Rev. Lett.* **98**, 227401 (2007).
- [60] A. Antognini, P. Crivelli, T. Prokscha, K. S. Khaw, B. Barbiellini, L. Liskay, K. Kirch, K. Kwuida, E. Morenzoni, F. M. Piegsa, Z. Salman, and A. Suter, Muonium emission into vacuum from mesoporous thin films at cryogenic temperatures, *Phys. Rev. Lett.* **108**, 143401 (2012).
- [61] T. Prokscha, E. Morenzoni, K. Deiters, F. Foroughi, D. George, R. Kobler, A. Suter, and V. Vrankovic, The new μE4 beam at PSI: A hybrid-type large acceptance channel for the generation of a high intensity surface-muon beam, *Nucl. Instrum. Methods Phys. Res., Sect. A* **595**, 317 (2008).
- [62] E. Morenzoni, F. Kottmann, D. Maden, B. Matthias, M. Meyerberg, T. Prokscha, T. Wutzke, and U. Zimmermann, Generation of very slow polarized positive muons, *Phys. Rev. Lett.* **72**, 2793 (1994).
- [63] T. Prokscha, E. Morenzoni, C. David, A. Hofer, H. Glückler, and L. Scandella, Moderator gratings for the generation of epithermal positive muons, *Appl. Surf. Sci.* **172**, 235 (2001).
- [64] E. Morenzoni, H. Glückler, T. Prokscha, H. P. Weber, E. M. Forgan, T. J. Jackson, H. Luetkens, C. Niedermayer, M. Pleines, M. Birke, A. Hofer, J. Litterst, T. Riseman, and G. Schatz, Low-energy μSR at PSI: present and future, *Physica B* **289–290**, 653 (2000).
- [65] Z. Salman, T. Prokscha, P. Keller, E. Morenzoni, H. Saadaoui, K. Sedlak, T. Shiroka, S. Sidorov, A. Suter, V. Vrankovic, and H.-P. Weber, Design and simulation of a spin rotator for longitudinal field measurements in the low energy muons spectrometer, *Phys. Proc.* **30**, 55 (2012).
- [66] More precisely, $N_{0,i}$ is proportional to the total number of muons implanted (i.e., the size of the spin ensemble) and b_i is the (virtually) time-independent count rate from muon-positron decays that are uncorrelated (see, e.g. [9]). Typically, b_i is $\sim 1\%$ of $N_{0,i}$.
- [67] At lower applied fields, it is possible to resolve the approximately degenerate Mu spin-precession frequencies in high-statistics measurements (cf. [13, 58, 59]).
- [68] Note that the field distribution in Nb is intrinsically Gaussian, but "narrows" to a Lorentzian under modest muon motion and gives rise to the exponential term in Equation (4) (see, e.g., [9]). When the depolarization rate is slow compared to the inverse muon lifetime (as in the case here), the form of the relaxation "envelope" for the two distribution types is nearly indistinguishable. Empirically, we find a slightly better fit is obtained if exponential depolarization is assumed.
- [69] A. Suter and B. M. Wojek, Musrfit: A free platform-independent framework for μSR data analysis, *Phys. Proc.* **30**, 69 (2012).
- [70] A. Suter, M. M. Martins, X. Ni, T. Prokscha, and Z. Salman, Low energy measurements in low-energy μSR , *J. Phys.: Conf. Ser.* **2462**, 012011 (2023).
- [71] C. Boekema, R. H. Heffner, R. L. Hutson, M. Leon, M. E. Schillaci, W. J. Kossler, M. Numan, and S. A. Dodds, Diffusion and trapping of positive muons in niobium, *Phys. Rev. B* **26**, 2341 (1982).
- [72] A. Maisuradze, A. Yaouanc, R. Khasanov, A. Amato, C. Baines, D. Herlach, R. Henes, P. Keppler, and H. Keller, Evidence for Cooper pair diffraction on the vortex lattice of superconducting niobium, *Phys. Rev. B* **88**, 140509(R) (2013).
- [73] T. Junginger, S. Calatroni, A. Sublet, G. Terenziani, T. Prokscha, Z. Salman, A. Suter, T. Proslie, and J. Zasadzinski, A low energy muon spin rotation and point contact tunneling study of niobium films prepared for superconducting cavities, *Supercond. Sci. Technol.* **30**, 125013 (2017).
- [74] H. K. Birnbaum, M. Camani, A. T. Fiory, F. N. Gygax, W. J. Kossler, W. Rüegg, A. Schenck, and H. Schilling, Anomalous temperature dependence in the depolarization rate of positive muons in pure niobium, *Phys. Rev. B* **17**, 4143 (1978).
- [75] M. Borghini, T. O. Niinikoski, J. C. Soulié, O. Hartmann, E. Karlsson, L. O. Norlin, K. Pernestål, K. W. Kehr, D. Richter,

- and E. Walker, Muon diffusion in niobium in the presence of traps, *Phys. Rev. Lett.* **40**, 1723 (1978).
- [76] Y. Krasnikova, A. A. Murthy, F. Crisa, M. Bal, Z. Sung, J. Lee, A. Cano, D. M. T. van Zanten, A. Romanenko, A. Grassellino, A. Suter, T. Prokscha, and Z. Salman, Magnetic fluctuations in niobium pentoxide, [arXiv:2312.10697 \[cond-mat.mtrl-sci\]](https://arxiv.org/abs/2312.10697).
- [77] To determine E^* , separate TRIM.SP simulations were required where the SiO₂ layer was omitted (see Appendix C) [13, 33].
- [78] J. H. Brewer, G. D. Morris, D. J. Arseneau, D. G. Eshchenko, V. G. Storchak, and J. Bermejo, Delayed muonium formation in quartz, *Physica B* **289–290**, 425 (2000).
- [79] G. A. Ausman Jr. and F. B. McLean, Electron-hole pair creation energy in SiO₂, *Appl. Phys. Lett.* **26**, 173 (1975).
- [80] This detail is accounted for in the muon-implantation simulations (see, e.g., [13, 45]).
- [81] E. B. Karlsson, The positive muon implanted in metals — a story full of surprises, *Eur. Phys. J. H* **39**, 303 (2014).
- [82] V. G. Storchak and N. V. Prokof'ev, Quantum diffusion of muons and muonium atoms in solids, *Rev. Mod. Phys.* **70**, 929 (1998).
- [83] For comparison, had we assumed our measurement was in the extreme motional-narrowing limit, Equation (8) reduces to $\lambda = 2\sigma^2/\nu$ (see, e.g., [9]) and $\nu = 4.8(4) \mu\text{s}^{-1}$, which differs from the more accurate estimate by 1.84(23).
- [84] D. N. Beshers, An investigation of interstitial sites in the bcc lattice, *J. Appl. Phys.* **36**, 290 (1965).
- [85] M. Asaduzzaman, R. M. L. McFadden, E. Thoeng, R. E. Laxdal, and T. Junginger, Measurements of the first-flux-penetration field in surface-treated and coated Nb: distinguishing between near-surface pinning and an interface energy barrier, *Supercond. Sci. Technol.* **37**, 085006 (2024).
- [86] M. Döbeli, C. Kottler, F. Glaes, and M. Suter, ERDA at the low energy limit, *Nucl. Instrum. Methods Phys. Res., Sect. B* **241**, 428 (2005).
- [87] M. Mayer, SIMNRA, a simulation program for the analysis of NRA, RBS and ERDA, *AIP Conf. Proc.* **475**, 541 (1999).
- [88] J. A. Phillips, The energy loss of low energy protons in some gases, *Phys. Rev.* **90**, 532 (1953).
- [89] H. K. Reynolds, D. N. F. Dunbar, W. A. Wenzel, and W. Whaling, The stopping cross section of gases for protons, 30–600 keV, *Phys. Rev.* **92**, 742 (1953).
- [90] J. E. Brolley and F. L. Ribe, Energy loss by 8.86-Mev deuterons and 4.43-Mev protons, *Phys. Rev.* **98**, 1112 (1955).
- [91] J. B. Swint, R. M. Prior, and J. J. Ramirez, Energy loss of protons in gases, *Nucl. Instrum. Methods* **80**, 134 (1970).
- [92] V. Dose and G. Sele, Das elektronische bremsvermögen von stickstoff und sauerstoff für niederenergetische protonen, *Z. Phys. A* **272**, 237 (1975).
- [93] R. A. Langley, Stopping cross sections for helium and hydrogen in H₂, N₂, O₂, and H₂S (0.3–2.5 MeV), *Phys. Rev. B* **12**, 3575 (1975).
- [94] F. Besenbacher, H. H. Andersen, P. Hvelplund, and H. Knudsen, Stopping power of swift hydrogen and helium ions in gases, *Mat. Fys. Medd. Dan. Vid. Selsk.* **40**, 3 (1979).
- [95] H. Baumgart, W. Arnold, H. Berg, E. Huttel, and G. Clausnitzer, Proton stopping powers in various gases, *Nucl. Instrum. Methods Phys. Res.* **204**, 597 (1983).
- [96] G. Reiter, H. Baumgart, N. Kniest, E. Pfaff, and G. Clausnitzer, Proton and helium stopping cross sections in N₂, O₂, NO and N₂O., *Nucl. Instrum. Methods Phys. Res., Sect. B* **27**, 287 (1987).
- [97] G. Reiter, N. Kniest, E. Pfaff, and G. Clausnitzer, Proton and helium stopping cross sections in H₂, He, N₂, O₂, Ne, Ar, Kr, Xe, CH₄ and CO₂, *Nucl. Instrum. Methods Phys. Res., Sect. B* **44**, 399 (1990).
- [98] N. Shiomi-Tsuda, N. Sakamoto, H. Ogawa, M. Tanaka, M. Saitoh, and U. Kitoba, Stopping powers of N₂ and O₂ for protons from 4.0 to 13.0 MeV, *Nucl. Instrum. Methods Phys. Res., Sect. B* **149**, 17 (1999).
- [99] W. F. v. d. W. C. Foster, W. H. Kool and H. E. Roosendaal, Random stopping power for protons in silicon, *Radiat. Eff.* **16**, 139 (1972).
- [100] F. Cembali and F. Zignani, Determination of random and aligned stopping powers for 80–300 keV protons in silicon by back-scattering measurements, *Radiat. Eff.* **31**, 169 (1977).
- [101] A. Carnera, G. D. Mea, A. V. Drigo, S. L. Russo, P. Mazzoldi, and G. G. Bentini, Channeled and random proton stopping power in the 30–1000 keV energy range, *Phys. Rev. B* **17**, 3492 (1978).
- [102] P. Gehrmann, K. Lenkeit, and R. Stolle, Measurements of proton channeling energy losses in silicon in the intermediate energy region, *Phys. Status Solidi B* **131**, 519 (1985).
- [103] C. Eppacher, Ph.D. thesis, Johannes Kepler Universität Linz, Linz, Austria (1994).
- [104] A. Ikeda, K. Sumitomo, T. Nishioka, and Y. Kido, Stopping powers and energy straggling for 50–300 keV H⁺ in amorphous Si and Ge films, *Nucl. Instrum. Methods Phys. Res., Sect. B* **115**, 34 (1996).
- [105] M. Famá, G. H. Lantschner, J. C. Eckardt, N. R. Arista, J. E. Gayone, E. Sanchez, and F. Lovey, Energy loss and angular dispersion of 2–200 keV protons in amorphous silicon, *Nucl. Instrum. Methods Phys. Res., Sect. B* **193**, 91 (2002).
- [106] G. Hobler, K. K. Bourdelle, and T. Akatsu, Random and channeling stopping power of H in Si below 100 keV, *Nucl. Instrum. Methods Phys. Res., Sect. B* **242**, 617 (2006).
- [107] M. Abdesselam, S. Ouichaoui, M. Azzouz, A. Chami, and M. Siad, Stopping of 0.3–1.2 MeV/u protons and alpha particles in Si, *Nucl. Instrum. Methods Phys. Res., Sect. B* **266**, 3899 (2008).
- [108] M. Brocklebank, S. N. Dedyulin, and L. V. Goncharova, Stopping cross sections of protons in Ti, TiO₂ and Si using medium energy ion scattering, *Eur. Phys. J. D* **70**, 248 (2016).
- [109] E. P. Arkhipov and Y. V. Gott, Slowing down of 0.5–30 keV protons in some materials, *Sov. Phys. JEPT* **29**, 615 (1969).
- [110] H. Grahmann and S. Kalbitzer, Nuclear and electronic stopping powers of low energy ions with $Z \leq 10$ in silicon, *Nucl. Instrum. Methods* **132**, 119 (1976).
- [111] W. H. Bragg and R. Kleeman, XXXIX. On the α particles of radium, and their loss of range in passing through various atoms and molecules, *Philos. Mag.* **10**, 318 (1905).